VNUHCM Journal of Science and Technology Development 2026, 29(2):4065-4073

Open Access Full Text Article

Research Article

Relationship between the microstructure, composition, and thermoelectric properties of Mg_2Sn thin films

Trang Thuy Thi Phan[1,2], Thu Minh Thi Nguyen[1,2,3], Quang Thua Trieu[1,2], Tran Le[2,3], Ngoc Van Le[2,3], Anh Tuan Thanh Pham[1,2,*]

ABSTRACT

Mg_2Sn-based semiconductors are promising candidates for electrical and thermoelectric device applications. Mg_2Sn is a narrow-bandgap semiconductor; however, its thin-film forms have not been extensively studied. In this study, Mg_2Sn films were deposited on glass substrates by co-sputtering with a fixed RF source for the Mg target and varying the DC sputtering power for the Sn target. The results demonstrate that variations in the Sn sputtering power influenced the structural properties, surface morphology, elemental composition, and thermoelectric properties of the resultant thin films. Specifically, the results revealed a structural transition from the cubic phase to a mixed cubic-orthorhombic phase at a sputtering power of 40 W, resulting in a near- stoichiometric Mg_2Sn composition. These two factors improved the thermoelectric properties of the Mg_2Sn films, reaching a power factor of 0.72 μW/m.K^2. However, the Seebeck coefficients of both films remained low, primarily caused by excess metallic phases.

Key words: Thermoelectrics, Mg2Sn, alloy thin films, sputtering

[1]*Laboratory of Advanced Materials, University of Science, Ho Chi Minh City, Vietnam*

[2]*Vietnam National University, Ho Chi Minh City, Vietnam*

[3]*Faculty of Physics and Engineering physics, University of Science, Ho Chi Minh City, Vietnam*

Correspondence

Anh Tuan Thanh Pham, Laboratory of Advanced Materials, University of Science, Ho Chi Minh City, Vietnam

Vietnam National University, Ho Chi Minh City, Vietnam

Email: pttanh@hcmus.edu.vn

History

- Received: 15-09-2025
- Revised: 09-01-2026
- Accepted: 06-02-2026
- Published Online: 02-06-2026

DOI : https://doi.org/10.32508/vnuhcmjstd.v29i2.4594

INTRODUCTION

Global energy demand has been steadily increasing, while conventional energy sources such as fossil fuels and coal are being rapidly depleted. Consequently, the development and optimization of renewable energy sources, including solar, wind, and biomass, have become essential for ensuring sustainable energy production and addressing future energy challenges. In this context, thermoelectric materials have emerged as promising candidates for mitigating the global energy shortage. Various classes of thermoelectric materials have been investigated, including oxides,[1] alloy-based compounds,[2] skutterudites,[3] and half-heusler materials.[4]

The performance of thermoelectric materials for practical applications is typically evaluated using the dimensionless figure of merit (ZT). Among these materials, Mg_2X (X = Si, Se, Sn)-based semiconductors with cubic antifluorite structures (space group: Fm3-m) have demonstrated relatively high ZT values, indicating strong potential for energy conversion applications.[5] These materials offer several advantages, including low cost, low toxicity, and natural abundance in the Earth's crust.[6] Furthermore, they possess an indirect band gap of approximately 0.3 eV, which allows for relatively high electrical conductivity and carrier mobility while maintaining a reasonable Seebeck coefficient, thereby contributing to a favorable power factor.[7]

Thin-film configurations have also attracted considerable interest for thermoelectric device applications due to their lightweight nature, mechanical flexibility, and low fabrication cost.[8]Various techniques have been employed for thin-film fabrication, including sputtering,[9]molecular beam epitaxy (MBE),[10]and metal-organic chemical vapor deposition (MOCVD).[11] Among these, magnetron sputtering is a simple method that offers precise thickness control, dense films, and flexible parameter adjustment. Tani et al.[12] reported that the substrate temperature during the sputtering process significantly influenced the Mg/Sn compositional ratio, as well as microstructural properties such as grain size and preferred orientation. In their study, a high power factor of 8.5 μW/(cm.K^2) at 519 K was achieved for films deposited at 523 K; these films featured the cubic Mg_2Sn phase with a minor Sn secondary phase. Safavi et al.[13] demonstrated that the DC sputtering power applied to the Sn target significantly affected the structural, morphological, and compositional characteristics of Mg_2Sn films. Their study revealed a phase transition from the stable fluorite cubic structure to a metastable orthorhombic structure, which markedly influenced the thermoelectric performance of the films. Specifically, the Mg_2Sn

Cite this article : Phan T T T, Nguyen T M T, Trieu Q T, Le T, Le N V, Pham A T T. **Relationship between the microstructure, composition, and thermoelectric properties of Mg_2Sn thin films**. *VNUHCM J. Sci. Technol. Dev.* 2026; 29(2):4065-4073.

films with the orthorhombic structure exhibited a ZT value of approximately 0.26 at 200°C. The development of an orthorhombic structure improves crystallinity and carrier mobility, leading to enhanced electrical conductivity. Previous studies have similarly reported that sputtering power has a significant influence on the structural characteristics, surface morphology, and the chemical composition of Mg_2Sn films—particularly in relation to phase formation, which directly governs their electrical conductivity and thermoelectric performance. [14,15]

However, achieving precise control over the phase formation of Mg_2Sn and minimizing excess metallic phases remain significant challenges, as the sputtering power directly influences the kinetic energy of atoms during film growth. Under vacuum conditions, collisions between Mg and Sn atoms can result in kinetic energy loss, making it difficult to accurately measure and control this energy. Consequently, Mg_2Sn films containing excess metallic phases typically exhibit high electrical conductivity but a reduced Seebeck coefficient. In light of this, optimizing sputtering power is a crucial step toward improving the thermoelectric performance of Mg_2Sn films, which demonstrate strong potential for practical applications. A deeper understanding of how sputtering power governs phase evolution and carrier transport is essential for the design of high-performance Mg_2Sn-based thermoelectric materials.

This study systematically examines the effects of sputtering power on the structural characteristics, surface morphology, elemental composition, and thermoelectric properties of Mg_2Sn thin films deposited via DC/RF co-sputtering.

MATERIALS AND METHODS

Mg-Sn films were deposited on glass substrates by DC/RF co-sputtering using a Leybold Univex-450 system. High-purity (99.99%) Mg and Sn metal targets (3-inch, Gredmann, Taiwan) were employed to fabricate the Mg_2Sn films. The chamber was evacuated to a base pressure of approximately 3.5×10^{-6} torr using a molecular pump before introducing Ar gas. All films were deposited under an Ar working pressure of 2 mtorr for 15 min at a substrate temperature of 300°C. The Mg target was powered at a constant 50 W using a 13.56 MHz RF source, while the Sn target was powered using a DC source at 30 W and 40 W.

The crystalline structure and phase composition of the films were analyzed by X-ray diffraction (XRD, Bruker D8-Advance, USA) using a monochromatic CuKα radiation source (λ = 0.1541 nm). Chemical composition was determined using an energy-dispersive X-ray spectroscopy (EDX, Horiba H-7593), while surface morphology was investigated using a field-emission scanning electron microscopy (FE-SEM, Hitachi S-4800). The Seebeck coefficient (S), electrical conductivity (σ), and power factor (PF) of the samples were measured as a function of temperature using a Linseis LSR-3 system. The resistivity and conductivity of the films were also measured using the digital four-point probe tester (JG ST2253).

RESULTS AND DISCUSSION

Figure 1a presents the XRD patterns of Mg_2Sn films deposited at different sputtering powers applied to the Sn target. All samples exhibit diffraction peaks at 2θ values of 22.76°, 26.37°, 37.63°, 44.39°, 54.22°, and 59.57°, which correspond to the (111), (200), (220), (311), (400), and (331) lattice planes of the cubic Mg_2Sn phase (JCPDS: 03-065-2997). [12] Among these peaks, the responses corresponding to the (111), (220), and (311) lattice planes of the cubic Mg_2Sn phase consistently exhibit higher intensities compared to the other diffraction peaks. Although the films deposited at Sn sputtering powers of 30 W and 40 W were Mg-rich, only a minor Mg phase was detected in the XRD patterns. This suggests that much of the excess Mg either exists in a non-crystalline form or is finely dispersed within the Mg_2Sn matrix. [16] In addition, diffraction peaks at 2θ values of 34.47° and 47.90° were also observed; these correspond to the (302) and (523) lattice planes of the orthorhombic Mg_2Sn phase (JCPDS: 00-031-0812). [13] The diffraction peak at 22.76°—which corresponds to the (111) lattice plane of the cubic Mg_2Sn phase—exhibits the highest intensity among all samples and remains relatively unaffected by changes in Sn sputtering power. At the initial 30 W sputtering power, only a very weak diffraction peak corresponding to the (302) lattice plane associated with the orthorhombic Mg_2Sn phase was observed. However, the intensity of this peak increased markedly as the Sn sputtering power was increased to 40 W, indicative of the possible formation of an orthorhombic phase coexisting with the cubic Mg_2Sn structure. Furthermore, the appearance of the orthorhombic phase in the 40 W film was accompanied by the formation of a secondary Sn phase, identified by the (200) plane at approximately 2θ = 37.15° (JCPDS: 03-065-0296). [13] These findings suggest that increasing the Sn sputtering power to 40 W provides the additional energy required to drive the orthorhombic Mg_2Sn phase, since it possesses a higher formation energy than the cubic phase. [16]

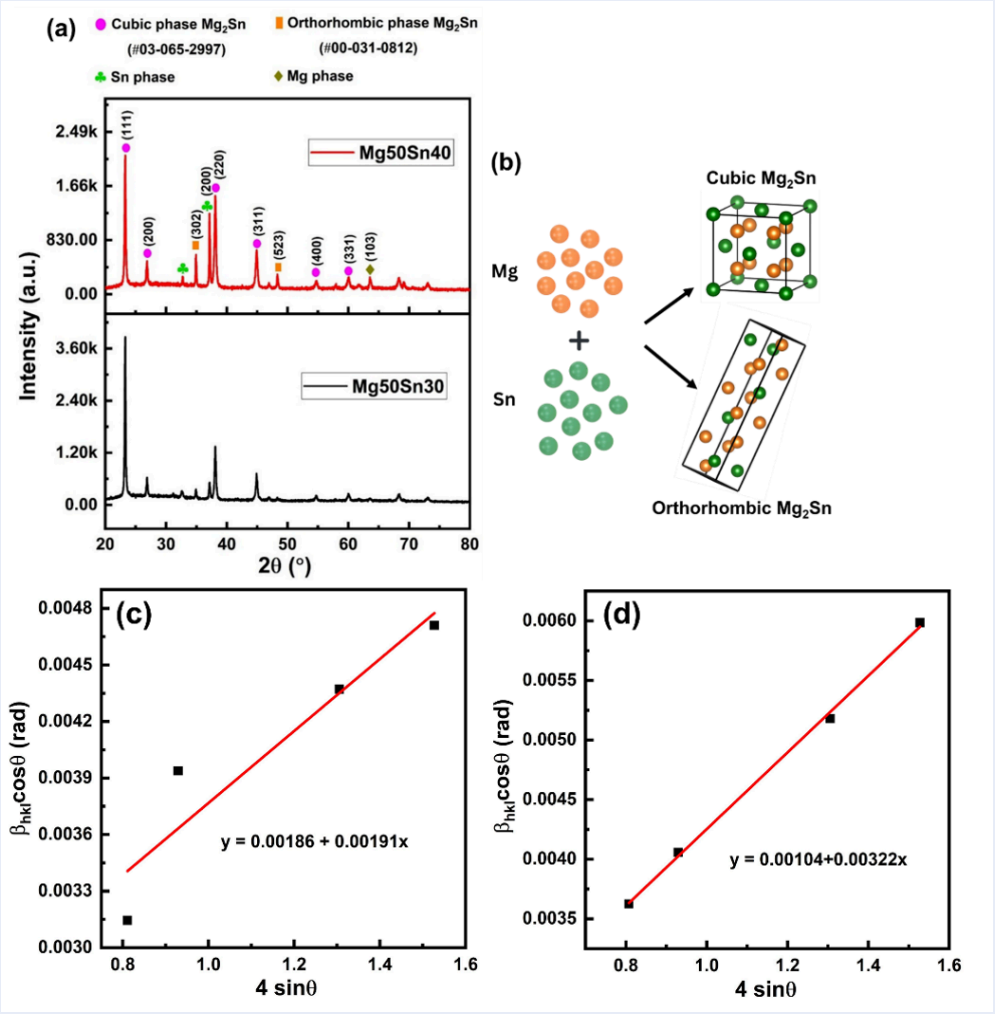

Figure 1: (a)XRD patterns of Mg_2Sn films with varying Sn sputtering power. (b) The crystal structure of the cubic and orthorhombic Mg_2Sn phases.(c-d) Williamson-Hall strain and crystalline size of cubic phase $Mg_2Sn$with Sn sputtering powers of 30 Wand 40 W, respectively.

Figure 1**b** presents the crystal structures of both the cubic and orthorhombic Mg_2Sn phases. The cubic phase has a fluorite-type structure (Fm-3m) with Mg atoms at fcc sites and Sn atoms in tetrahedral interstitial positions, forming a highly symmetric and stable structure under equilibrium conditions. In contrast, the orthorhombic phase (Pnma) possesses a lower-symmetry, metastable structure characterized by distorted Mg-Sn bonding that forms under higher-energy conditions; this significantly influences the electronic structure and carrier transport properties of the material.

Typically, a phase transition occurs at the transition pressure (i.e., the point at which the enthalpies of the two phases become equal), with the most stable phase corresponding to the phase with the lowest energy.[17] Our results indicate that a sputtering power of 40 W was sufficient to reach this transition point, facilitating phase transformation without the need for additional treatments such as annealing or external pressure. These results are consistent with previous studies that suggested a phase transition from the cubic to the orthorhombic structure induced by variations in Sn sputtering power.[13] Furthermore, earlier studies have shown that increasing the Sn sputtering power can induce changes in lattice defects depending on the symmetry of these defects, the structure may be driven toward either higher or lower symmetry states.[13]

To gain further insights into the structural evolution of the Mg_2Sn films, the crystallite sizes of the domi-

nant phases were estimated using the Scherrer equation, defined as $D = 0.9\lambda/\beta\cos\theta$,[18] where D, β, and θ represent the crystallite size, the full width at half maximum (FWHM), and the diffraction angle, respectively. The calculated crystallographic parameters of the Mg_2Sn films are summarized in Table 1.

The FWHM of the cubic Mg_2Sn phase increases with sputtering power, suggesting a degradation in its crystalline quality. Conversely, the FWHM of the orthorhombic Mg_2Sn phase at the (302) plane and metallic Sn phase decreased with increasing power, indicating an increase in crystallinity.

The average crystallite size of the cubic Mg_2Sn phase was approximately 35.1 nm for the 30 W film; this decreased to 30.6 nm for the 40 W film. Similarly, the average crystallite size of the orthorhombic Mg_2Sn phase decreased from 49.9 nm (30 W) to 43.9 nm (40 W). However, the crystallite size of the (302) lattice plane in the orthorhombic phase increased markedly from 41.2 nm to 50.2 nm, indicative of a significant improvement in its local crystallinity. The average crystallite size of the Sn phase also increased significantly, from 30.0 nm in the 30 W film to 49.9 nm in the 40 W film.

The broadening of diffraction peaks is generally associated with both crystallite size and lattice strain. According to the Williamson–Hall (W–H) method, the total peak broadening (β_{hkl}) can be expressed as the sum of two contributions as follows[19]:

$$\beta_{hkl} = \beta_D + \beta_\varepsilon$$

where β_D represents the peak broadening due to finite crystallite size and β_ε corresponds to the broadening caused by lattice strain, which arises from crystal defects and distortions. Assuming the lattice strain in the material is uniform in all crystal phase directions according to the uniform deformation model, β_D and β_ε can be calculated by the following expression:

$$\beta_D = \frac{k\lambda}{D\cos\theta}$$
$$\beta_\varepsilon = 4\varepsilon\ \tan\theta$$

This equation can be rearranged into the following form:

$$\beta_{hkl}\ \cos\theta = \frac{k\lambda}{D} + 4\varepsilon\ \sin\theta$$

Accordingly, the slope and y-intercept of the fitted Williamson–Hall plot correspond to the lattice strain and crystallite size, respectively (Figure 1**c-d**). The average crystallite size of the Mg_2Sn cubic phase in the Mg50Sn30 film was approximately 74.5 nm with a corresponding strain of 4.78×10^{-3}. In contrast, the Mg50Sn40 film exhibited a larger average crystallite size of 133.3 nm and a significantly lower strain of 0.85×10^{-3}.

It should be noted that the crystallite sizes estimated using the Debye–Scherrer and Williamson-Hall methods differ. This discrepancy arises because the Williamson–Hall method accounts for both crystallite size and lattice microstrain, whereas the Debye-Scherrer equation considers only crystalline size broadening. The substantial reduction in strain for the Mg50Sn40 film indicates a more stable crystal lattice with less distortion and a lower defect density, leading to improved crystallinity and enhanced grain growth.

Despite the cubic-to-orthorhombic phase transformation, the presence of excess metallic Mg and Sn phases was detected in both films. Previous studies have reported the formation of an Mg_2Sn phase via a peritectic reaction at approximately 561°C,[20] a temperature that is considerably higher than the deposition temperature used in this study (300°C). Under such conditions, the diffusion between Mg and Sn atoms is limited, preventing the formation of a fully homogeneous Mg_2Sn phase and causing excess metallic Mg and Sn to remain within the films.

Furthermore, earlier work has shown that increasing the Sn atomic concentration during Mg_2Sn film deposition at 350°C led to the emergence of excess metallic Sn,[13] evidenced by the appearance of a secondary Sn phase with the (200) lattice plane. This observation is consistent with the results of this study, which reveals the presence of an Sn phase corresponding to the (002) lattice plane at a sputtering power of 40 W.

SEM analyses were performed to evaluate the influence of Sn sputtering power on the surface morphology of Mg_2Sn alloy films (Figure 2**a-b**). Both films exhibited uniform coverage over the substrate. The film deposited at 30 W exhibited small and closely-clustered particles, while the 40W film contained larger grains.

The grain structure of the Mg_2Sn films was further investigated by calculating the grain size distribution of both films (Figure 2**c-d**). The average grain sizes of the films deposited at 30 W and 40 W were 1.81 μm and 3.37 μm, respectively. The larger grain size of the 40W film (nearly twice that of the 30W film) suggests that higher sputtering powers promote grain growth and improved crystallinity.

This structural analysis suggests the coexistence of cubic and orthorhombic phases at higher sputtering power, accompanied by an increase in grain size. This indicates that the emergence of the orthorhombic phase contributed to improved film crystallinity

Table 1: Crystallographic parametersof Mg_2Sn films under different Sn sputtering powers.

Samples	Phase	Cubic phase Mg2Sn				Orthorhombic phase Mg2Sn		Sn phase	
	Lattice	(111)	(200)	(220)	(311)	(302)	(523)	x	(200)
Mg50Sn30	2θ (o)	23.29	26.87	38.10	44.89	34.91	48.34	32.59	37.15
	FWHM (o)	0.184	0.232	0.265	0.292	0.202	0.149	0.347	0.231
	D (nm)	44.08	35.23	31.75	29.38	41.24	58.56	23.87	36.21
Mg50Sn40	2θ (o)	23.29	26.87	38.10	44.91	34.93	48.32	32.69	37.13
	FWHM (o)	0.212	0.239	0.314	0.371	0.166	0.231	0.151	0.187
	D (nm)	38.31	34.21	26.72	23.16	50.19	37.64	54.97	44.86

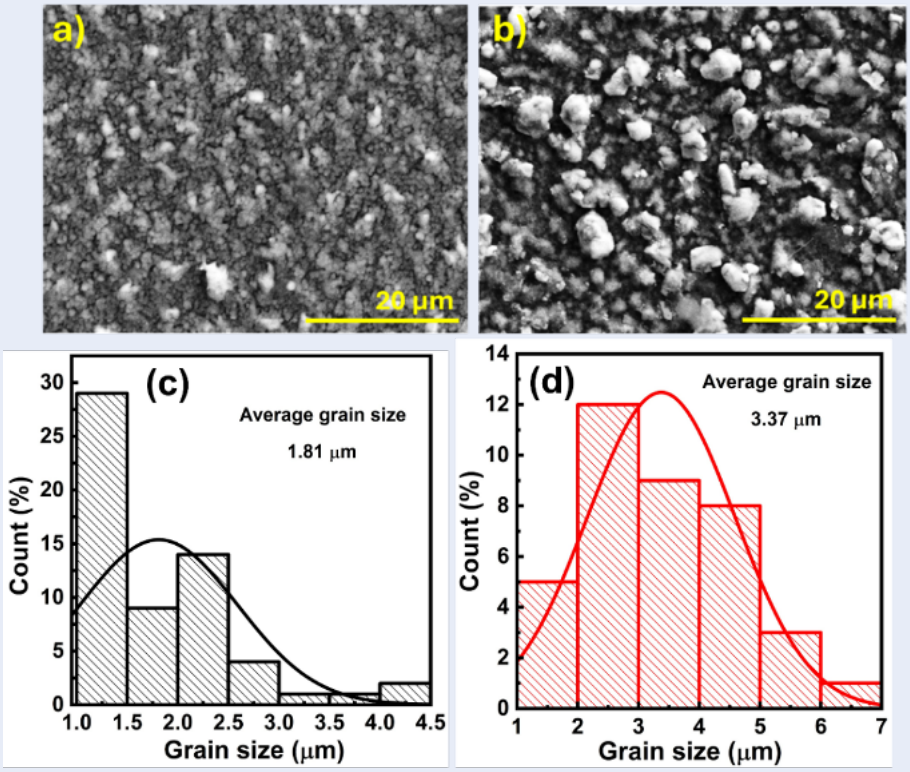

Figure 2: (a, b) Surface morphology and (c, d) corresponding grain sizedistribution of the Mg50Sn30 and Mg50Sn40 films.

because of higher formation energy compared to the cubic phase. Furthermore, the increase in grain size and crystallinity at higher Sn sputtering power promotes more efficient carrier transport by minimizing grain boundary scattering. This consequently enhances the electrical conductivity and contributes to the improved thermoelectric performance of the Mg_2Sn films.

The effect of sputtering power on the chemical composition of Mg_2Sn films was investigated using EDS analyses; these results are presented in Figure 3 and Table 2. The EDS spectra in Figure 3**a** confirm the presence of Mg and Sn elements without detectable impurities. The relative peak intensity of Sn increases with increasing Sn sputtering power, indicating a higher Sn content in the Mg50Sn40 film. The film deposited at 40 W (Figure 3 **b**) exhibited an Mg/Sn ratio of 1.85, close to the stoichiometric ratio of Mg_2Sn (2:1). In contrast, the film sputtered at 30 W possessed a much higher Mg content with an Mg/Sn ratio of

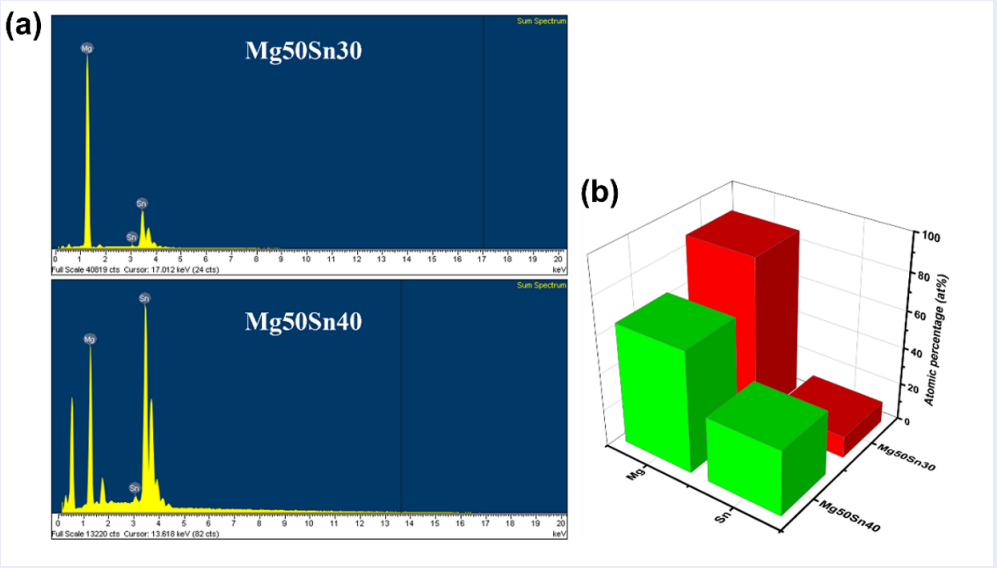

Figure 3: (a)EDS spectra of Mg and Sn elements. (b) Elemental composition ratios of Mg_2Sn films deposited at Sn sputtering powers of 30 W and 40 W.

7.63. Due to the lower atomic mass of Mg compared to Sn, the former is sputtered more efficiently under Ar^+ bombardment, resulting in an Mg-rich film. These findings show that a Sn sputtering power of 40 W allows for better control over the stoichiometric composition of Mg_2Sn.

Notably, the XRD data reveal the coexistence of orthorhombic and cubic Mg_2Sn phases in the 40 W film, together with excess metallic Sn and Mg. The Mg/Sn ratio of this film is close to the thermodynamically stable stoichiometry of Mg_2Sn, which facilitates the formation of both phases.

Table 2: Chemical composition of Mg_2Sn alloythin films fabricated at different Sn sputtering powers.

Samples	Elemental composition	% atoms (at.%)	Mg/Sn ratio
Mg50-Sn30	Mg	88.42	7.63
	Sn	11.58	
Mg50-Sn40	Mg	64.89	1.85
	Sn	35.11	

The thermoelectric properties of the Mg_2Sn films as a function of Sn sputtering power are presented in Figure 4. Specifically, the conductivity of the films was measured as a function of temperature (Figure 4**a**). The conductivity of all Mg_2Sn films gradually decreased as the temperature increased from room temperature to 580 K. At room temperature, the film deposited at 30 W exhibited a conductivity of 1.2×10^3 S/cm, while the 40 W film exhibited a much higher conductivity of 9.4×10^3 S/cm—this trend persisted across the entire temperature range. The enhanced conductivity of the film fabricated at 40 W is attributed to its near-stoichiometric composition, which suppresses the formation of native defects such as Mg-related vacancies and interstitials. Such defects are common in Mg_2Sn films due to their low formation energies; consequently, reducing their concentration directly improves the intrinsic conductivity of the films.[21]

The possible emergence of the orthorhombic Mg_2Sn phase may also contribute to enhanced electrical conductivity due to its more favorable electronic band structure for charge carrier transport.[22] The enhanced crystallinity observed in the 40 W film compared to the 30 W film can also improve carrier transport, consistent with the XRD and EDS results.

Four-point probe measurements were carried out to further assess the electrical transport properties of the Mg_2Sn films. The resistivity of the Mg_2Sn films was determined to be 7.5×10^{-4} Ω.cm and 1.1×10^{-4} Ω.cm for the films sputtered at 30 W and 40 W, respectively, corresponding to an increase in electrical conductivity from 1.3×10^3 S/cm for the 30W film to 9.0×10^3 S/cm for the 40W film. These results show that there is a significant improvement in charge

transport with increasing sputtering power, consistent with the conductivity obtained from thermoelectric measurements. Wataru et al.[23] reported that the conductivity of Sb-doped Mg_2Sn films reached 5.0×10^3 S/cm at room temperature.

Figure 4**b** shows that both alloy films exhibit an increasing Seebeck coefficient with increasing temperature. However, despite the films retaining the Mg_2Sn crystal structure, the Seebeck values remain very low, ranging from -1.2 to -3.6 μV/K. Such low values are consistent with degenerate semiconductor-like (i.e., near-metallic) behavior, which may be related to the high carrier concentration associated with excess Mg and Sn phases.

Although the 40 W film exhibited significantly higher electrical conductivity than the 30 W film, their Seebeck coefficients were relatively similar. This behavior suggests that the high conductivity of the 40 W film can be attributed to the enhanced crystallinity of the 40W film, which promotes more efficient electron transport. Consequently, the increased conductivity of the 40 W film primarily arises from reduced grain boundary scattering rather than a substantial change in carrier concentration, resulting in only minor differences in the Seebeck coefficient between the two films.

At room temperature, the Seebeck coefficients of the two films are nearly identical; however, the coefficients of both films increase gradually with temperature, with a more pronounced rise in the 40 W film at 590 K. This enhancement can be attributed to the coexistence of cubic and orthorhombic Mg_2Sn phases in the 40 W sample, which exhibits a higher crystallinity and improved thermoelectric response. Furthermore, the increase in the Seebeck coefficient at elevated temperatures, particularly around 590 K, may be associated with the formation of Mg vacancies. At high temperatures, Mg atoms can easily evaporate or diffuse out of the lattice, leading to the formation of numerous Mg vacancies. These defects reduce the carrier concentration, thereby increasing the Seebeck coefficient according to the Pisarenko relation. This interpretation is consistent with previous studies that reported the formation of Mg-vacancy-related defects in Mg_2Sn films.[23]

Figure 4**c** presents the temperature-dependent power factor of Mg_2Sn films deposited at different Sn sputtering powers. The power factor of both films increases with temperature, reaching 0.4 μW/m.K^2 and 0.72 μW/m.K^2 at 590 K for the 30 W and 40 W films, respectively. The improved performance of the 40 W film can be attributed to its higher electrical conductivity and slightly improved Seebeck coefficient, which in turn is due to its near-stoichiometric composition and the coexistence of cubic and orthorhombic Mg_2Sn phases.

The Seebeck coefficient of the Mg_2Sn films is low, leading to a low power factor. Indeed, the obtained power factor is lower than that of Mg_2Sn single crystals (11 μW/m.K^2) and Mg_2Sn films prepared by co-sputtering (260 μW/m.K^2),[16,24] as well as Ga-doped Mg_2Sn (1.49 mW/m.K^2).[7] Future work should focus on enhancing the Seebeck coefficient through compositional tuning and post-deposition treatments, while simultaneously maintaining the high electrical conductivity of the material to achieve improved thermoelectric performance.

CONCLUSION

This study demonstrates that Sn sputtering power plays a crucial role in governing the structural, compositional, morphological, and thermoelectric characteristics of Mg_2Sn films. Increasing the Sn sputtering power to 40 W triggers a phase transition from the stable cubic phase to a mixed cubic-orthorhombic structure, which is accompanied by significant changes to the microstructure and properties of the film. Specifically, the 40 W film exhibits larger and more densely packed grains, indicative of improved crystallinity, and achieves an Mg/Sn ratio close to the ideal stoichiometric composition. This near-stoichiometric ratio suppresses the formation of defects such as Mg vacancies or interstitials, thereby improving charge carrier mobility and electrical conductivity. As a result, the film deposited at 40 W has a power factor of 0.72 μW/m.K^2 at 590 K.

Nevertheless, this study is limited by the absence of thermal conductivity measurements, while the overall thermoelectric performance is hindered by the material's metallic-like Seebeck coefficients, which are likely caused by excess metallic phases. Future work should focus on investigating the effects of deposition and post-annealing temperatures on the complete formation of the Mg_2Sn phase, as well as the reduction of excess metallic phases. These improvements should improve the Seebeck coefficient, resulting in enhanced overall thermoelectric performance.

ACKNOWLEDGEMENTS

This research is funded by Vietnam National University, Ho Chi Minh City (VNU-HCM) under grant number B2025-18-03.

COMPETING INTERESTS

The authors declare that they have no competing interests.

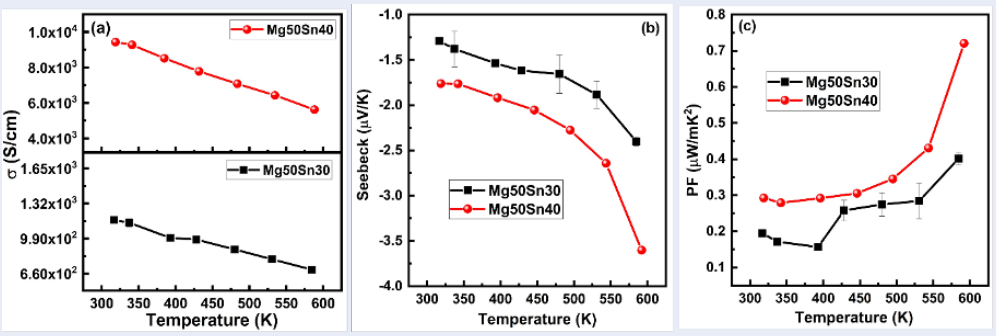

Figure 4: Temperaturedependence of (a) electrical conductivity, (b) Seebeck coefficient, and (c)power factor for Mg_2Sn films deposited at Sn sputtering powers of 30W and 40 W.

AUTHORS' CONTRIBUTIONS

T.T.T. Phan: Data curation, Investigation, Formal analysis, Writing – original draft. T.M.T. Nguyen: Data curation, Investigation. Q.T. Trieu: Data curation. T. Le: Data curation, Methodology. N.V. Le: Data curation, Methodology. A.T.T. Pham: Conceptualization, Supervision, Funding acquisition, Writing – review & editing.

REFERENCES

1. Ji L. Metal oxide-based thermoelectric materials. Metal Oxides in Energy Technologies. Elsevier Inc.; 2018. Available from: https://doi.org/10.1016/b978-0-12-811167-3.00003-1.
2. Fatima N, Karimov KS, Qasuria TA, Ibrahim MA. A novel and stable way for energy harvesting from Bi2Te3Se alloy based semitransparent photo-thermoelectric module. Journal of Alloys and Compounds. 2020;849. Available from: https://doi.org/10.1016/j.jallcom.2020.156702.
3. Pan H, Sun Z, Geng H, Chang Q, Zhang B, Zhang L. Thermal stability optimization of single-leg skutterudite-based thermoelectric devices based on lattice distortion effects. Journal of Materiomics. 2025;11(2). Available from: https://doi.org/10.1016/j.jmat.2024.02.015.
4. Mitra M, Benton A, Akhanda MS, Qi J, Zebarjadi M, Singh DJ, et al. Conventional Half-Heusler alloys advance state-of-the-art thermoelectric properties. Materials Today Physics. 2022;28. Available from: https://doi.org/10.1016/j.mtphys.2022.100900.
5. Liu Y, Song G, Li G, Wu Y, Du H, You J. Thin films of thermoelectric Mg2Sn containing nano-sized metal Sn phase by magnetron sputtering. Chemical Physics Letters. 2022;788. Available from: https://doi.org/10.1016/j.cplett.2021.139305.
6. Song G, Liu Y, Ran L, Shao Y, Hu F, Wu Y, et al. The layered growth and thermoelectric properties of the Mg2Sn films. Thin Solid Films. 2022;748. Available from: https://doi.org/10.1016/j.tsf.2022.139175.
7. Lima MS, Aizawa T, Ohkubo I, Baba T, Sakurai T, Mori T. High power factor in epitaxial Mg2Sn thin films via Ga doping. Applied Physics Letters. 2021;119(25). Available from: https://doi.org/10.1063/5.0074707.
8. Phan TT, Le OK, Nguyen LT, Duong YN, Le MT, Lai HT, et al. Defect modification in enhancing thermopower factor of ZnO films without doping. Ceramics International. 2024;50(17):30683–9. Available from: https://doi.org/10.1016/j.ceramint.2024.05.368.
9. Le-Quoc H, Lacoste A, Hlil EK, Bès A, Vinh TT, Fruchart D, et al. Thin films of thermoelectric compound Mg2Sn deposited by co-sputtering assisted by multi-dipolar microwave plasma. Journal of Alloys and Compounds. 2011;509(41):9906–11. Available from: https://doi.org/10.1016/j.jallcom.2011.07.085.
10. Aizawa T, Ohkubo I, Lima MS, Sakurai T, Mori T. Fabrication of Mg2Sn(111) film by molecular beam epitaxy. Journal of Vacuum Science; Technology A, Vacuum, Surfaces, and Films. 2019;37(6). Available from: https://doi.org/10.1116/1.5122844.
11. Gonzalez-Juarez MDL, Flores E, Martin-Gonzalez M, Nandhakumar I, Bradshaw D. Electrochemical deposition and thermoelectric characterisation of a semiconducting 2-D metal-organic framework thin film. Journal of Materials Chemistry A, Materials for Energy and Sustainability. 2020;8(26):13197–206. Available from: https://doi.org/10.1039/D0TA04939E.
12. Tani J, Ishikawa H, undefined Tani J-ichi. Ishikawa H. Thermoelectric properties of Mg2Sn thin films fabricated using radio frequency magnetron sputtering. Thin Solid Films. 2019;692. Available from: https://doi.org/10.1016/j.tsf.2019.137601.
13. Safavi M, Martin N, Linseis V, Palmino F, Cherioux F, Billard A, et al. Thermoelectric properties improvement in Mg2Sn thin films by structural modification. Journal of Alloys and Compounds. 2019;797:1078–85. Available from: https://doi.org/10.1016/j.jallcom.2019.05.214.
14. Liu X, Shan D, Song Y, Chen R, Han E. Influences of the quantity of Mg2Sn phase on the corrosion behavior of Mg–7Sn magnesium alloy. Electrochimica Acta. 2011;56(5):2582–90. Available from: https://doi.org/10.1016/j.electacta.2010.12.030.
15. Cui Y, Jiang T, Zhu S, Dong T, Wei L, Si J. Strong texture in nanostructured thin films Mg2Sn leads to superior thermoelectric performance. Journal of Alloys and Compounds. 2025;1030. Available from: https://doi.org/10.1016/j.jallcom.2025.180807.
16. Kim S, Kim NH. Electronic structure and thermoelectric properties of Mg2Sn films fabricated by using co-sputtering process with stoichiometric modification. IEEE;Available from: https://doi.org/10.1109/ACCESS.2021.3137868.
17. Yu F, Sun JX, Chen TH. High-pressure phase transitions of Mg2Ge and Mg2Sn: first-principles calculations. Phys. B. Physica B, Condensed Matter. 2011;406(9):1789–94. Available from: https://doi.org/10.1016/j.physb.2011.02.029.
18. Fang C, Wen Z, Liu X, Hao H, Chen G, Zhang X. Microstructures and mechanical properties of Mg2Sn-nanophase reinforced Mg2Sn composite. Materials Science and Engineering A. 2017;684:229–32. Available from: https://doi.org/10.1016/j.msea.2016.12.001.
19. Butt MZ, Ali D, Farooq H, Bashir F. Structural, electrical, and mechanical characteristics of proton beam irradiated Al5086 alloy. Phys. B. Physica B, Condensed Matter. 2015;456:275–82. Available from: https://doi.org/10.1016/j.physb.2014.09.014.
20. Nayeb-Hashemi AA, Clark JB. The Mg-Sn (Magnesium-Tin) system. Bulletin of Alloy Phase Diagrams. 1984;5(5):466–76. Available from: https://doi.org/10.1007/BF02872898.

21. Duparchy A, Deshpande R, Sankhla A, Ghosh S, Camut J, Park S, et al. Instability mechanism in thermoelectric Mg2(Si,Sn) and the role of Mg diffusion at room temperature. Small Science. 2024;5(3). Available from: https://doi.org/10.1002/smsc.202300298.
22. Chen CL, Chen SC, Chou CL, Wang TH, Chuang MC, Tang BC, et al. Enhanced thermoelectric performance of Mg–Sn thin films: Role of Mg9Sn5 phase and one-dimensional electronic structure. ACS Applied Materials; Interfaces. 2024;16(3):3520–31. Available from: https://doi.org/10.1021/acsami.3c17226.
23. Saito W, Hayashi K, Huang Z, Dong J, Li JF, Miyazaki Y. Enhancing the thermoelectric performance of Mg2Sn single crystals via point defect engineering and Sb doping. ACS Applied Materials; Interfaces. 2020;12(52):57888–97. Available from: https://doi.org/10.1021/acsami.0c17462.
24. Saito W, Hayashi K, Dong J, Li JF, Miyazaki Y. Control of the thermoelectric properties of Mg2Sn single crystals via point-defect engineering. Scientific Reports. 2020;10(1):2020. Available from: https://doi.org/10.1038/s41598-020-58998-1.